

Complex resonance absorption structure in the X-ray spectrum of IRAS 13349+2438*

M. Sako¹, S. M. Kahn¹, E. Behar¹, J. S. Kaastra², A. C. Brinkman², Th. Boller³, E. M. Puchnarewicz⁴, R. Starling⁴, D. A. Liedahl⁵, J. Clavel⁶, and M. Santos-Lleo⁶

¹ Department of Physics and Columbia Astrophysics Laboratory, 550 West 120th Street, New York, NY 10027, USA

² Space Research Organization of the Netherlands, Sorbonnelaan 2, 3548 CA, Utrecht, The Netherlands

³ Max-Planck-Institut fuer Extraterrestrische Physik, Postfach 1603, 85741 Garching, Germany

⁴ Mullard Space Science Laboratory, University College, London, Holmbury St. Mary, Dorking, Surrey, RH5 6NT, UK

⁵ Physics Department, Lawrence Livermore National Laboratory, PO Box 808, L-41, Livermore, CA 94550, USA

⁶ XMM Science Operations, Astrophysics Division, ESA Space Science Dept., PO Box 50727, 28080 Madrid, Spain

Received 2 October 2000 / Accepted 30 October 2000

Abstract. The luminous infrared-loud quasar IRAS 13349+2438 was observed with the *XMM-Newton* Observatory as part of the Performance Verification program. The spectrum obtained by the Reflection Grating Spectrometer (RGS) exhibits broad ($v \sim 1400 \text{ km s}^{-1}$ FWHM) absorption lines from highly ionized elements including hydrogen- and helium-like carbon, nitrogen, oxygen, and neon, and several iron L-shell ions (Fe XVII–XX). Also shown in the spectrum is the first astrophysical detection of a broad absorption feature around $\lambda = 16\text{--}17 \text{ \AA}$ identified as an unresolved transition array (UTA) of 2p–3d inner-shell absorption by iron M-shell ions in a much cooler medium; a feature that might be misidentified as an O VII edge when observed with moderate resolution spectrometers. No absorption edges are clearly detected in the spectrum. We demonstrate that the RGS spectrum of IRAS 13349+2438 exhibits absorption lines from at least two distinct regions, one of which is tentatively associated with the medium that produces the optical/UV reddening.

Key words. atomic processes – line: formation – techniques: spectroscopic – quasars: absorption lines – quasars: individual: IRAS 13349+2438 – X-rays: galaxies

1. Introduction

IRAS 13349+2438 is an archetypal highly-polarized radio-quiet quasar at a redshift of $z = 0.10764$ (Kim et al. 1995). Since its identification as an infrared-luminous quasar (Beichman et al. 1986), this source has been extensively studied in the optical, infrared, and X-ray bands. In a detailed investigation of the optical and infrared spectra and polarization measurements, Wills et al. (1992) demonstrated that the nuclear spectrum exhibits two distinct components; a highly-reddened component and a highly-polarized component that suffers much lower extinction. Based on these observational facts, Wills (1992) constructed a simple and elegant picture of the nuclear

region of IRAS 13349+2438 in which the direct AGN radiation is attenuated by a thick dusty torus, while the observed highly-polarized light is produced by scattering in an extended bipolar region, either by warm electrons or by small dust grains.

IRAS 13349+2438 was detected in the *ROSAT* All-Sky-Survey (Walter & Fink 1993; Brinkmann & Siebert 1994), and has been the target of extensive pointed PSPC observations with *ROSAT* (Brandt et al. 1996), and with *ASCA* (Brinkmann et al. 1996; Brandt et al. 1997). The soft X-ray spectrum obtained with the PSPC shows a lack of absorption by cold material indicated by the observed optical reddening, and suggests the presence of a warm, dusty medium along the line of sight (Brandt et al. 1996).

In a more recent investigation of the complex X-ray properties of IRAS 13349+2438, Siebert et al. (1999) self-consistently accounted for the effects of dust embedded in the warm absorbing medium, and concluded that single zone models, both with and without internal dust, do not

Send offprint requests to: M. Sako,
 e-mail: masao@astro.columbia.edu

* Based on observations obtained with *XMM-Newton*, an ESA science mission with instruments and contributions directly funded by ESA Member States and the USA (NASA).

provide adequate fits to the combined, *ROSAT*, *ASCA*, and optical data sets. In particular, they find that a dust-free warm absorber model formally gives the best fit to the X-ray data, and conclude that the X-ray absorption and optical reddening must arise in spatially distinct regions. However, owing to the moderate spectral-resolving-power capabilities of the available detectors on *ROSAT* and *ASCA*, and the likely cross-calibration uncertainties, the precise nature of the soft X-ray spectrum has remained controversial.

In this Letter, we present results from the first high-resolution X-ray observation of IRAS 13349+2438 with the *XMM-Newton* Observatory. The spectrum obtained with the Reflection Grating Spectrometer (RGS) shows a wealth of discrete spectral features, including the first astrophysical detection of inner-shell 2p–3d absorption by M-shell iron ions in the form of an unresolved transition array (UTA). From a detailed analysis of the rich absorption spectrum, we measure the column density and velocity field of the line-of-sight material. We show that the spectrum contains absorption features from regions with two distinct levels of ionization. The column density of the lower ionization component is consistent with the observed optical reddening, and we tentatively associate this component with the dusty torus.

2. Observation and data reduction

IRAS 13349+2438 was observed with the *XMM-Newton* observatory (Jansen et al. 2001) on 19–20 June, 2000 during the Performance Verification phase for a total exposure time of 42 ks. The data obtained with the Reflection Grating Spectrometer (RGS; den Herder et al. 2001) were filtered through standard event-selection criteria using the *XMM-Newton* Science Analysis Software (SAS). The source spectrum was extracted using a spatial filter in dispersion/cross-dispersion coordinates to isolate IRAS 13349+2438 from other possible contaminating sources and to reduce contribution from background events. Subsequently, the first order events were selected by applying a dispersion/pulse-height filter. The background spectrum was generated using all of the events that lie outside the spatial mask. Wavelengths were then assigned to the dispersion coordinates. The current wavelength scale is accurate to within ~ 8 mÅ across the entire RGS band of $\lambda = 5\text{--}35$ Å ($E = 0.35\text{--}2.5$ keV).

The European Photon Imaging Camera (EPIC; Turner et al. 2001; Stüder et al. 2001) MOS1 data were also processed with the SAS. The MOS2 detector was operated in FAST UNCOMP mode, for which reduction by the SAS is not possible as yet. Source events were extracted using a circular region of radius $45''$. A nearby source-free region with a radius of $3'$ was used to assess the background.

Three modes of the Optical Monitor (OM; Mason et al. 2000) were used during the observation. The *V* grism (or optical grism; exposure time 3000 s), *UV* grism (exposure time 1000 s), and the UVW2 filter ($\sim 1500\text{--}3000$ Å; effective exposure time 6340 s). There is no significant

variability in the UVW2 observations. Absolute flux calibrations for the grism data were not available at the time of writing. The optical spectrum shows clear evidence of H β emission but the signal-to-noise is insufficient to determine the presence of any other emission lines (within an observer frame wavelength range of $\sim 3000\text{--}6000$ Å). The *UV* spectrum (coverage $\sim 2000\text{--}3500$ Å) is too weak for spectral extraction.

3. Results of spectral fitting

3.1. Underlying continuum radiation

To first obtain a rough characterization of the shape of the continuum, we use the PN spectrum, which has the highest statistical quality and covers a broad range in energy. During the observation, the source exhibited a gradual and steady increase in brightness by $\sim 30\%$, but with no noticeable change in the spectral shape. We, therefore, use the cumulative spectrum for all of our subsequent analyses. The 0.2–10 keV spectral region can be well-fitted with a phenomenological model that consists of a powerlaw and two black body components absorbed through a Galactic column density of $N_{\text{H}}^{\text{gal}} = 1.1 \cdot 10^{20} \text{ cm}^{-2}$ (Murphy et al. 1996). The PN data require two black body components with temperatures of $kT \sim 70$ eV and ~ 12 eV. The best-fit powerlaw photon index of $\Gamma \sim 2.2$ is consistent with the value implied by the *ASCA* data (Brinkmann et al. 1996; Brandt et al. 1997).

The MOS1 data from 0.3 to 10 keV, excluding the 0.6–1.2 keV region where the RGS shows complex absorption features, were best-fit using a single blackbody plus power-law (a χ_r^2 of 1.59 for 199 degrees of freedom), which is generally consistent with the PN data. The blackbody temperature is $kT \sim 110$ eV. The best-fit photon index is $\Gamma = 2.1$ with a column density of $1.4 \cdot 10^{20} \text{ cm}^{-2}$, which is only slightly higher than the Galactic value.

3.2. The absorption spectrum of IRAS 13349+2438

The RGS spectrum shown in Fig. 1 exhibits numerous absorption lines from a wide range in levels of ionization. The most prominent features in the spectrum are K-shell absorption lines of H- and He-like carbon, nitrogen, oxygen, and neon, and L-shell lines of Fe xvii–xx. The spectrum also shows a broad absorption feature between $\lambda \sim 16\text{--}17$ Å ($E \sim 730\text{--}770$ eV). The observed location of the red “edge” of this feature is at $\lambda = 17.10 \pm 0.05$ Å in the rest-frame of the quasar, and is close but undoubtedly inconsistent with that of the O vii photoelectric edge ($\lambda = 16.78$ Å). The shape of the absorption trough towards the shorter wavelengths is also incompatible with that of a photoelectric edge. We identify this feature as a UTA of inner-shell 2p–3d resonance absorption lines in relatively cool, M-shell iron. The shape of this feature is strikingly similar to laboratory absorption measurements of a heated iron foil (Chenais-Popovics et al. 2000), and

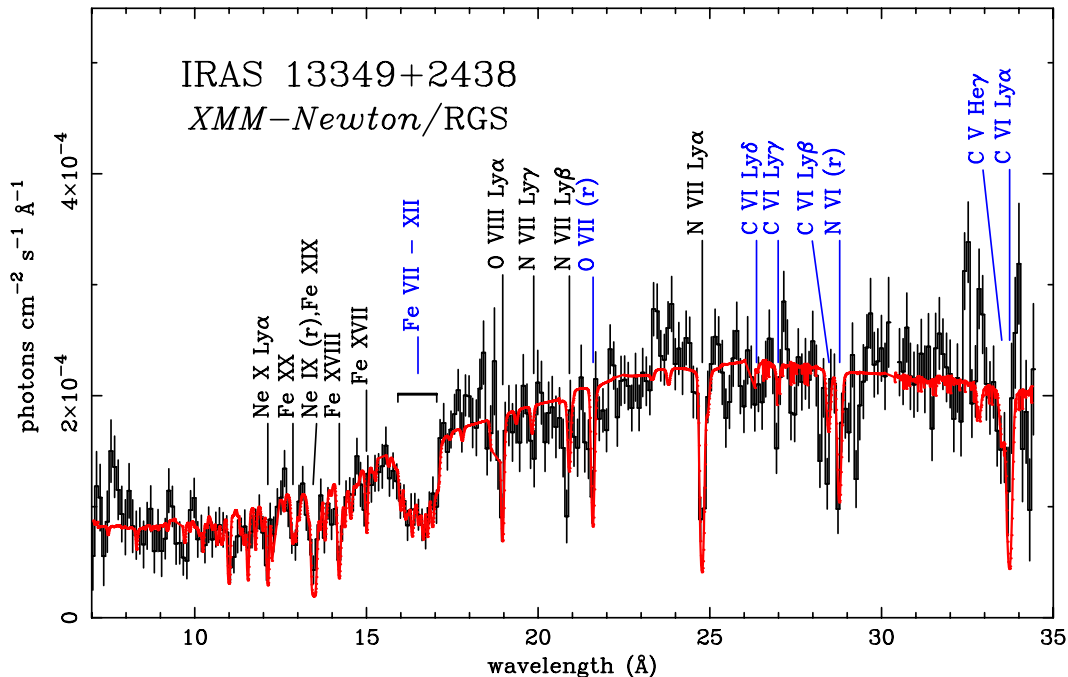


Fig. 1. The RGS first order spectrum of IRAS 13349+2438 corrected for cosmological redshift ($z = 0.10764$). The error bars represent 1σ Poisson fluctuations. The wavelength bins are approximately ~ 0.1 Å wide. The best-fit model spectrum is superimposed in red. Absorption line features labeled in blue are predominantly produced in the low- ξ component, while those labeled in black originate from the high- ξ component (see text for full details). The discrepancy at $\lambda \sim 29.3$ Å is probably due to inner-shell absorption by N V (lithium-like), which is not included in our model

also agrees well with our own calculations as described below.

We adopt a continuum model similar to that inferred from the PN data; i.e., the sum of a powerlaw and a blackbody component, the latter merely in order to parametrize empirically the soft X-ray spectral shape. We also fix the powerlaw photon index to $\Gamma = 2.2$ and the column density of cold material to the Galactic value. With the continuum model defined, we then apply absorption components of H- and He-like C, N, O, and Ne, and Fe XVII–XXIV. Each ion is treated as a separate component in the spectral fit and contains all relevant resonance transitions from the ground-state and photoelectric edges in the RGS band. The line profiles are calculated accounting for thermal and turbulent velocity broadening. Transition wavelengths and oscillator strengths were calculated with the atomic physics package HULLAC (Bar-Shalom et al. 1998), except for the wavelengths of the strong Fe L resonance lines where we use laboratory measurement values described in Brown et al. (2000). We use photoionization cross sections from Verner et al. (1996). For the iron UTA absorption, photoexcitation cross sections from L-shell to M-shell in Fe V – XVI are computed. All of the transitions $2l^8 3l^x - 2l^7 3l^{x+1}$ ($x = 1$ through 12) are taken into account, of which the 2p–3d excitations are the most important. For the atomic structure, the most significant configuration mixings, which conserve the total angular momentum within the $n = 3$ shell (namely $3p^2 + 3s3d$), are included. This approximation is expected to be adequate for analysing the presently observed unresolved absorption feature. A more

detailed discussion of the UTA is presented in Behar et al. (2000).

Each component is then convolved through the instrument line spread function and fit for the ion column density simultaneously with the black body continuum parameters and the normalization of the powerlaw component. The best-fit black body temperature is $kT \sim 100$ eV with a flux in the 5–35 Å range of $4.0 \cdot 10^{-3}$ photons $\text{cm}^{-2} \text{s}^{-1}$. The flux in the powerlaw component is $2.4 \cdot 10^{-3}$ photons $\text{cm}^{-2} \text{s}^{-1}$ in the same wavelength range.

The observed widths of the absorption lines, as shown below, are much larger than both the instrument line spread function and the thermal broadening of a gas with $kT \sim 10$ eV, which is the expected temperature for a photoionized plasma at this level of ionization. With the current statistical quality of the RGS data, however, we are not able to constrain the turbulent velocities v_{turb} of the individual ion components. We, therefore, assume a uniform mean turbulent velocity field, keeping in mind that each ion can, in principle, exist in regions of different turbulent velocities. The derived ion column densities, therefore, may be uncertain to some degree, as quantified in the following section.

We obtain a statistically acceptable fit to the RGS data with $\chi^2_{\nu} = 1.07$ for 532 degrees of freedom. The continuum parameters inferred from the RGS data are also consistent with those derived from PN and MOS. The intrinsic isotropic luminosities in the 0.3–2 keV and 2–10 keV regions are $L_X \sim 2 \cdot 10^{44}$ erg s^{-1} and $\sim 5 \cdot 10^{43}$ erg s^{-1}

Table 1. Measured ion column densities

Ion	N_i (cm $^{-2}$) ^a	$\Delta\chi^2$ ^b	Component ^c
C V	$(6.3^{+5.2}_{-4.8}) 10^{16}$	4.8	low
C VI	$(6.0^{+6.4}_{-3.1}) 10^{16}$	23.7	low
N VI	$(2.4^{+1.4}_{-1.0}) 10^{16}$	29.1	low
N VII	$(1.3^{+0.8}_{-0.4}) 10^{17}$	109.5	low/high
O VII	$(3.7^{+1.7}_{-1.3}) 10^{16}$	24.2	low
O VIII	$(9.5^{+8.7}_{-4.7}) 10^{16}$	24.7	high
Ne IX	$(1.2^{+0.6}_{-0.5}) 10^{18}$	9.9	high
Ne X	$(4.9^{+10}_{-3.2}) 10^{17}$	25.9	high
Fe XVII	$(1.7^{+1.6}_{-1.2}) 10^{17}$	23.0	high
Fe XVIII	$(6.3^{+2.4}_{-1.9}) 10^{17}$	115.0	high
Fe XIX	$(9.7^{+4.8}_{-3.9}) 10^{17}$	166.7	high
Fe XX	$(3.0^{+2.8}_{-2.0}) 10^{17}$	39.5	high
Fe VII	$(1.5^{+1.5}_{-1.3}) 10^{16}$	9.6	low
Fe VIII	$(4.6^{+1.5}_{-1.3}) 10^{16}$	91.8	low
Fe IX	$(8.8^{+12}_{-8.7}) 10^{15}$	29.3	low
Fe X	$(2.4^{+1.3}_{-1.1}) 10^{16}$	72.4	low
Fe XI	$(1.9^{+1.1}_{-0.9}) 10^{16}$	65.3	low
Fe XII	$(6.4^{+10}_{-4.4}) 10^{16}$	25.6	low

^a The turbulent velocities for all of the ions are fixed to the same value. We find a best-fit with $v_{\text{turb}} = 1430^{+360}_{-280}$ km s $^{-1}$ FWHM.

^b The increase in χ^2 when the ion component is excluded from the best-fit model.

^c The dominant ξ -component responsible for producing the absorption feature (see Fig. 1 and text for details).

(assuming $H_0 = 65$ km s $^{-1}$ Mpc $^{-1}$ and $q_0 = 0.5$), respectively, which are lower than both the *ROSAT* PSPC and *ASCA* values by a factor of ~ 5 . The measured ion column densities are listed in Table 1. To illustrate the statistical significance of the various components, we also list the changes in χ^2 when each of the components is removed from the model. The best-fit FWHM turbulent velocity is $v_{\text{turb}} = 1430^{+360}_{-280}$ km s $^{-1}$, which is much larger than the thermal velocity of a photoionized medium. We also find weak evidence of an average bulk outflow velocity shift with $v_{\text{shift}} = +200^{+170}_{-180}$ km s $^{-1}$, where positive velocity denotes a blueshift.

4. Implications of the results of spectral fitting

For the measured ion column densities listed in Table 1, many of the strong absorption lines of neon and iron L ions are in the logarithmic region of the curves of growth, which indicates that the derived column densities are highly coupled with the assumed turbulent velocity. Those of K-shell carbon, nitrogen, and oxygen, and iron M-shell ions, however, are in the linear regime, and the derived column densities are not very sensitive to the turbulent velocity. An important point to note is that the observed velocity widths may as well be due to a superposition of multiple, discrete absorption components each of which are optically thin, and are unresolved with the RGS. Such

features have been observed in UV absorption line spectra of many Seyfert 1 galaxies (Crenshaw et al. 1999, and references therein), some of which show as many as 7 distinct, kinematic components (e.g., Mrk 509; Kriss et al. 2000). If this is the case, the measured column densities from the neon and iron L lines, which are produced in the logarithmic region of the curve of growth, may be underestimated relative to the true value. The column densities of the He-like species, as well as those of the UTA, are not affected by this, since the total observed values are still in the optically thin regime.

As shown in Table 1, the detections of absorption lines from Fe VII–XII and Fe XVII–XX are highly significant. The column densities of the intermediate charge states of Fe XIII–XVI, however, are consistent with zero, with an upper limit of $N_i \sim \text{few } 10^{15}$ cm $^{-2}$ for each of these charge states. This indicates that the line-of-sight material consists of either a multi-phase gas in a single medium, or two (or more) spatially distinct regions. Motivated by this observational fact, we refit the spectrum using the same model, except, we assume that the line-of-sight material consists of two discrete velocity components; (1) the low-ionization-parameter component including C VI, C V, N VI, O VII, and the M-shell Fe, and (2) the high-ionization-parameter component including N VII, O VIII, Ne IX, Ne X, and L-shell Fe. Contrary to our previous fit where the bulk velocities of all the ions were fixed relative to one another, we find that the low-ionization-parameter component is significantly blue-shifted with $v_{\text{shift,low}} = +420^{+190}_{-180}$ km s $^{-1}$, while the bulk velocity shift in the high-ionization component is consistent with zero ($v_{\text{shift,high}} = -20^{+200}_{-330}$ km s $^{-1}$). This implies that the low-ionization gas is being accelerated substantially compared to the high-ionization component, as would be expected in a radiatively-driven outflow (Arav & Li 1994). The derived turbulent velocities of both components remain consistent with that of our previous fit ($v_{\text{turb}} \sim 1500$ km s $^{-1}$ FWHM).

From the observed distribution of charge states of M-shell iron, the average ionization parameter, $\xi = L/nr^2$ (erg cm s $^{-1}$), of the absorbing gas is estimated to be $\log \xi \sim 0$ based on a calculation with the photoionization code XSTAR (Kallman & Krolik 1995) using the inferred continuum shape for the ionizing spectrum. The width of the distribution in ionization parameter is no larger than $\Delta \log \xi \sim 1$. The measured iron ion column densities suggest that the corresponding equivalent hydrogen column density is $N_{\text{H}} \sim (1 - 3) 10^{21}$ cm $^{-2}$ assuming a solar iron abundance. This low- ξ gas accounts for most of the carbon and He-like nitrogen and oxygen absorption lines as well, however, with some indication of lower carbon and nitrogen abundances by a factor of ~ 2 and oxygen by a factor of ~ 3 relative to the solar iron abundance. The lack of absorption from Fe XIII – XVI, however, indicates that substantial amounts of material with ionization parameters in the range $1 \lesssim \log \xi \lesssim 2$ are not present along the line-of-sight. Whether this is related to the global

structure of the circumnuclear medium or a mere coincidence from a superposition of physically distinct regions is not known.

The absorption lines from H-like nitrogen and oxygen, H- and He-like neon, and L-shell iron are produced in a medium with $2.0 \lesssim \log \xi \lesssim 2.5$ and an equivalent hydrogen column density of $N_{\text{H}} \sim (1 - 4) 10^{22} \text{ cm}^{-2}$, again, assuming a solar iron abundance. The inferred abundances of nitrogen, oxygen, and neon relative to that of iron are consistent with solar values, but are not well-constrained.

For a normal dust-to-gas ratio, the observed reddening of $E(B - V) = 0.3$ in IRAS 13349+2438 (Wills et al. 1992) corresponds to a hydrogen column density of $N_{\text{H}} = 1.7 10^{21} \text{ cm}^{-2}$ (Burstein & Heiles 1978). This value is significantly lower than the total amount of X-ray absorbing material (low- ξ + high- ξ) observed in the present X-ray spectrum. Coincidentally, however, the derived column density of the low- ξ component is very close to that of the optical reddening, although, we cannot conclusively associate the low- ξ X-ray absorber with the dusty torus. The column density of the high- ξ component, on the other hand, is a factor of ~ 10 higher.

An interesting point to note is that the $1 \lesssim \log \xi \lesssim 2$ region is *not* thermally unstable, based on XSTAR calculations described above. On the other hand, the high- ξ region ($2.0 \lesssim \log \xi \lesssim 2.5$) that we observe in the spectrum *is* thermally unstable. However, complications such as non-solar metal abundances and/or inaccurate ionization and recombination rates may alter the shape of the thermal stability curve significantly, and, hence, the temperature ranges of the unstable regions (Hess et al. 1997; Savin et al. 1999).

For the observed X-ray luminosity of $L_{\text{X}} \sim 2.5 10^{44} \text{ erg s}^{-1}$, the high- ξ component with $\log \xi \gtrsim 2.0$ provides the constraint, $n_e r^2 \lesssim 2.5 10^{42} \text{ cm}^{-1}$. The measured column density through this medium is $N_{\text{H}} \sim n_e \Delta r \gtrsim 10^{22} \text{ cm}^{-2}$, where Δr is the radial thickness. Assuming that $\Delta r/r < 1$, these constraints combined provide an upper limit in the location of the high- ξ gas of $r_{\text{high-}\xi} < 2.5 10^{20} \text{ cm} \sim 80 \text{ pc}$, which is representative of a typical narrow-line region. The corresponding gas density in this region is $n_e \gtrsim 40 \text{ cm}^{-3}$ with an estimated thickness of $\Delta r \sim 80 \text{ pc} \sim r_{\text{high-}\xi}$. A similar calculation for the low- ξ component does not provide a useful constraint with $r_{\text{low-}\xi} < 10^{23} \text{ cm} \sim 3 \text{ kpc}$, and, therefore, the location of the low- ξ component is not well-determined compared to that of the high- ξ component. If the low- ξ component lies beyond the high- ξ component relative to the central continuum source, the difference in the measured bulk velocity shifts of the two components might indicate that the high- ξ gas is the base of an accelerating outflow. If, on the other hand, the low- ξ absorber is indeed spatially coincident with the torus, in which case $r_{\text{low-}\xi}$ is likely to be approximately the location of the broad-line region ($r_{\text{low-}\xi} \sim r_{\text{BLR}} \sim 1 \text{ pc}$), the medium is decelerating as a function of radius. Such a behavior has been observed in the UV spectrum of the Seyfert 1 galaxy NGC 4151 (Crenshaw et al. 2000).

As briefly mentioned earlier, the source during the present *XMM-Newton* observation was in an unusually low state. However, since the estimated location and density of the absorbing medium are such that the gas does not respond immediately to the observed continuum radiation (i.e., low density gas at large distances), the effect on the physical state of the absorbing medium by a variable illuminating source is not clear. It will be useful to re-observe IRAS 13349+2438 during a substantially brighter state to see whether the spectrum exhibits any dramatic changes in the absorption structures, and specifically if the oxygen absorption edges detected in the *ROSAT* and *ASCA* data (Brandt et al. 1996; Brandt et al. 1997) are really present during a different state. A detailed comparison of the UV and X-ray absorption spectra will also be interesting, particularly for identifying discrete kinematic components, as well as for constraining the global characteristics and dynamics of the absorbing medium.

5. Comparisons with other AGNs

The absorption spectrum of IRAS 13349+2438 is qualitatively similar to those obtained with the *Chandra* transmission grating observations of the Seyfert 1 galaxies NGC 5548 and NGC 3783, which show narrow absorption lines blue-shifted by several hundred km s^{-1} (Kaastra et al. 2000; Kaspi et al. 2000). The derived ion column densities in these sources, as well as in IRAS 13349+2438, are in the range $N_i \sim 10^{16} - 10^{17} \text{ cm}^{-2}$, and are not high enough to produce observable absorption edges.

Conceptually, the low-ionization component observed in IRAS 13349+2438 is similar to the “lukewarm absorber” that explains both the observed optical and X-ray attenuation in NGC 3227 (Kraemer et al. 2000). The spectroscopic signatures, however, are very different. In particular, for the column densities derived from the IRAS 13349+2438 data, the absorption features are dominated by discrete resonance line transitions, mainly in He-like ions and M-shell iron, and not by photoelectric edges as in the model of Kraemer et al. (2000).

As demonstrated in our detailed spectral analysis of IRAS 13349+2438, the UTA feature is potentially a powerful diagnostic tool for probing cool absorbing material using high-resolution X-ray observations. If the low-ionization component is indeed associated with the dusty torus as the derived column density suggests, this feature should be detectable in other AGNs where the line-of-sight is partially obscured by the torus.

Acknowledgements. We thank the referees N. Brandt and S. Gallagher for constructive comments that helped improve the quality of the manuscript. The Columbia University team is supported by NASA. The Laboratory for Space Research Utrecht is supported financially by The Netherlands Organization for Scientific Research (NWO). Work at LLNL was performed under the auspices of the U.S. Department of Energy by the University of California Lawrence Livermore National Laboratory under contract No. W-7405-Eng-48.

References

- Arav, N., & Li, Z.-Y. 1994, *ApJ*, 427, 700
- Bar-Shalom, A., Klapisch, M., Goldstein, W. H., & Oreg, J. 1998, the HULLAC code for atomic physics, unpublished
- Behar, E., Sako, M., & Kahn, S. M. 2001, in preparation
- Beichman, C. A., Soifer, B. T., Helou, G., et al. 1986, *ApJ*, 308, L1
- Boroson, T. A., & Meyers, K. A. 1992, *ApJ*, 397, 442
- Brandt, W. N., Fabian, A. C., & Pounds, K. A. 1996, *MNRAS*, 278, 326
- Brandt, W. N., Mathur, S., Reynolds, C. S., & Elvis, M. 1997, *MNRAS*, 292, 407
- Brinkmann, W., Kawai, N., Ogasaka, Y., & Siebert, J. 1996, *A&A*, 316, L9
- Brinkmann, W., & Siebert, J. 1994, *A&A*, 285, 812
- Brown, G. V., Beiersdorfer, P., Liedahl, D. A., Widmann, K., & Kahn, S. M. 2000, LLNL preprint, UCRL-JC-136647
- Burstein, D., & Heiles C. 1978, *ApJ*, 225, 40
- Chenais-Popovics, C., Merdji, H., Missalla, T., et al. 2000, *ApJS*, 127, 275
- Crenshaw, D. M., Kraemer, S. B., Bogges, A., Maran, S. P., Mushotzky, R. F., & Wu, C.-C. 1999, *ApJ*, 516, 750
- Crenshaw, D. M., Kraemer, S. B., Hutchings, J. B., et al. 2000, *AJ*, 120, 1731
- den Herder, J. W., Brinkman, A. C., Kahn, S. M., et al. 2001, *A&A*, 365, L7
- Hess, C. J., Kahn, S. M., & Paerels, F. B. S. 1997, *ApJ*, 478, 94
- Jansen, F., Lumb, D., Altieri, B., et al. 2001, *A&A*, 365, L1
- Kaastra, J. S., Mewe, R., Liedahl, D. A., Komossa, S., & Brinkman, A. C. 2000, *A&A*, 354, L83
- Kallman, T. R., & Krolik, J. H. 1995, XSTAR – A Spectral Analysis Tool, HEASARC, NASA/GSFC, Greenbelt
- Kaspi, S., Brandt, W. N., Netzer, et al. 2000, *ApJ*, 535, L17
- Kim, D.-C., Sanders, D. B., Veilleux, S., Mazzarella, J. M., & Soifer, B. T. 1995, *ApJS*, 98, 129
- Kraemer, S. B., George, I. M., Turner, T. J., & Crenshaw, D. M. 2000, *ApJ*, 535, 53
- Kriss, G. A., Green, R. F., Brotherton, M., et al. 2000, *ApJ*, 538, L17
- Mason, K. O., Breeveld, A., Much, R., et al. 2001, *A&A*, 365, L36
- Murphy, E. M., Lockman, F. J., Laor, A., & Elvis, M. 1996, *ApJS*, 105, 369
- Savin, D. W., et al. 1999, *ApJS*, 123, 687
- Siebert, J., Komossa, S., & Brinkmann, W. 1999, *A&A*, 351, 893
- Strüder, L., Briel, U., Dennerl, K., et al. 2001, *A&A*, 365, L18
- Turner, M. J. L., Abbey, A., Arnaud, M. et al. 2001, *A&A*, 365, L27
- Verner, D. A., Ferland, G. J., Korista, K. T., & Yakovlev, D. G. 1996, *ApJ*, 465, 487
- Walter, R., & Fink, H. H. 1993, *A&A*, 274, 105
- Wills, B. J., Wills, D., Evans, N. J., et al. 1992, *ApJ*, 400, 96